

Geophysical Research Letters

RESEARCH LETTER

10.1029/2018GL077997

Key Points:

- First airborne evaluation of snowfall property retrievals using triple-frequency radar and microphysical measurements
- A limited fraction of coincident points show nonspheroidal scattering behavior, challenging the value of differentiating particle type
- Bulk statistics of effective density and characteristic size support the retrieval hypotheses in previous literature

Supporting Information:

- Supporting Information S1

Correspondence to:

R. J. Chase,
randyjc2@illinois.edu

Citation:

Chase, R. J., Finlon, J. A., Borque, P., McFarquhar, G. M., Nesbitt, S. W., Tanelli, S., et al. (2018). Evaluation of triple-frequency radar retrieval of snowfall properties using coincident airborne in situ observations during OLYMPEx. *Geophysical Research Letters*, 45, 5752–5760. <https://doi.org/10.1029/2018GL077997>

Received 19 MAR 2018

Accepted 23 MAY 2018

Accepted article online 30 MAY 2018

Published online 12 JUN 2018

Evaluation of Triple-Frequency Radar Retrieval of Snowfall Properties Using Coincident Airborne In Situ Observations During OLYMPEx

Randy J. Chase¹ , Joseph A. Finlon¹ , Paloma Borque¹, Greg M. McFarquhar², Stephen W. Nesbitt¹, Simone Tanelli³, Ousmane O. Sy³, Stephen L. Durden³, and Michael R. Poellot⁴

¹Department of Atmospheric Sciences, University of Illinois at Urbana-Champaign, Urbana, IL, USA, ²Cooperative Institute of Mesoscale Meteorological Studies and School of Meteorology, University of Oklahoma, Norman, OK, USA, ³Jet Propulsion Laboratory, California Institute of Technology, Pasadena, CA, USA, ⁴Department of Atmospheric Sciences, University of North Dakota, Grand Forks, ND, USA

Abstract Scattering models of precipitation-size ice particles have shown that aggregates and spheroidal particles occupy distinct regions of the K_u - K_a - W -band dual-frequency ratio (DFR) plane. Furthermore, past ground-based observations suggest that particle bulk density and characteristic size can be retrieved from the DFR plane. This study, for the first time, evaluates airborne DFR observations with coincident airborne microphysical measurements. Over 2 hr of microphysical data collected aboard the University of North Dakota Citation from the Olympic Mountains Experiment are matched with Airborne Precipitation and cloud Radar Third Generation triple-frequency radar observations. Across all flights, 31% (63%) of collocated data points show nonspheroidal (spheroidal) particle scattering characteristics. DFR observations compared with in situ observations of effective density and particle characteristic size reveal relationships that could potentially be used to develop quantitative dual- and triple-frequency DFR ice property retrievals.

Plain Language Summary Currently, remote sensing retrievals of ice clouds require assumptions since particle shape and size vary greatly in the atmosphere. Additionally, particle shape and size constrain relationships of mass and fall velocity of ice within a cloud, which affect remote sensing retrievals. Modeling studies have shown that the scattering characteristics of complex ice particles (e.g., aggregates) have a distinct signature compared to spherical representations of the same particles when using three frequencies under the following conditions: (1) at least one radar with its wavelength close to the size of the particle and (2) particles have low effective densities. Thus, there is potential to retrieve information about particle shape using triple-frequency radar observations to constrain the assumptions of particle shape in the ice cloud retrieval. This paper is the first study to use airborne triple-frequency radar observations coincident with airborne in situ microphysical measurements to evaluate both the scattering signal discussed and retrievals of characteristic size and effective density. We found that 31% (63%) of the observations from the Olympic Mountains Experiment show nonspheroidal (spheroidal) scattering characteristics. Furthermore, the triple-frequency observations confirm the relationships with observed particle size and effective density outlined in a previous study supporting future use of triple-frequency missions.

1. Introduction

The development of active and passive satellite precipitation remote sensing has allowed for the characterization of weather systems around the world, including over the ocean and less populated areas where ground-based measurements are sparse. Spaceborne radar enables the retrieval of cloud and precipitation structure that is valuable for evaluating numerical model simulations (e.g., Delanoë et al., 2011; Stein et al., 2015). Furthermore, the retrieval of precipitation rate of ice (R) and ice water content (IWC) can characterize the global distribution of ice-phase precipitation, which is needed to understand the global water and energy budget. The retrieval of R and IWC requires assumptions about particle shape, size, mass, and particle terminal fall velocity. The use of multiple radar frequencies, one predominantly in the Rayleigh scattering regime and at least one in the Mie regime, has been investigated to constrain assumptions made in R and IWC retrievals. Kneifel et al. (2011) found that scattering models of complex particles such as low-density unrimed aggregates and dendrites occupy distinct regions of the triple-frequency dual-frequency ratio (DFR) K_u - K_a (DFR $_{Ku-Ka}$) and K_a - W (DFR $_{Ka-W}$) two-dimensional phase space when compared to models of soft spheres

and spheroids. Models of dendrites and aggregates with various monomers (e.g., Leinonen & Moisseev, 2015; Leinonen & Szyrmer, 2015; Petty & Huang, 2010) have shown that as the particle maximum dimension (D_{\max}) increases, there is an increase then a decrease of DFR_{Ka-W} while DFR_{Ku-Ka} increases continually. This creates a *hook* signature (e.g., see scattering curves in Figure 2 or Figure 3) in the triple-frequency DFR plane. Dissimilarly, using soft spheres and spheroid models (e.g., Austin et al., 2009; Matrosov, 2007) results in a continual increase of both DFR_{Ka-W} and DFR_{Ku-Ka} with increasing D_{\max} and, therefore, no *hook* signature (e.g., see polygon in Figure 2 or Figure 3). Thus, the triple-frequency DFR plane can be potentially used to determine regions dominated by nonspheroidal scattering behavior (e.g., unrimed aggregates) versus regions characterized by spheroidal scattering behavior (e.g., rimed particles).

Moreover, a portion of the triple-frequency observations collected over Wakasa Bay, Japan could be explained by the *hook* produced from aggregate and dendrite scattering models (Kulie et al., 2014; Leinonen et al., 2012). Despite the importance of these results, direct in situ evaluation of the inferences from scattering models of aggregates has remained largely elusive. One exception however, is the recent study by Kneifel et al. (2015), which used a surface disdrometer and triple-frequency range gates within 200 m of the surface to compare snowfall characteristics with triple-frequency signatures in southern Finland. When aggregates were observed at the surface, DFR values followed the *hook* of the aggregate and dendrite models, whereas when spherical particles were seen, the DFR values followed those respective models. Despite this first claim of consistency between scattering models and observed DFR, more testing of the triple-frequency phase space is needed for different particle habits, which depend on variable meteorological conditions where varying microphysical processes may dominate.

Additional bulk microphysical quantities such as effective bulk density (ρ_e) and characteristic particle size have been suggested as viable retrievals from the DFR plane. Analysis of ground based in situ observations have shown that higher ρ_e results in increased DFR_{Ka-W} and decreased DFR_{Ku-Ka} , effectively rotating the DFR curve (Kneifel et al., 2015). Furthermore, a recent modeling study (Leinonen & Szyrmer, 2015) varying the degree of riming on aggregates showed quasi-consistent results with the study of Kneifel et al. (2015) regarding larger amounts of rime ice and, thus, larger ρ_e , leading to higher DFR_{Ka-W} and little to no change in DFR_{Ku-Ka} . While these studies provide some evidence to support bulk microphysical retrievals, additional observations aloft and in different regimes are still necessary for a more thorough evaluation.

The Olympic Mountains Experiment (OLYMPEX), conducted in late 2015 over the west coast of the United States, in Washington State and the nearby coastal region (Houze et al., 2017), obtained triple-frequency airborne radar observations coincident with airborne in situ cloud microphysical measurements. In this study, these observations are used to determine if scattering models produce consistent results on the K_u - K_a - W -band DFR plane for various regions of stratiform clouds, which have ice particles of varying habits and sizes. Observations from OLYMPEX provide 2.2 hr of in-cloud data with K_u -, K_a -, and W -band radar observations coincident with in situ aircraft data characterizing particles and their bulk properties.

2. Methodology

2.1. Radar

To provide radar data coincident with in situ microphysics observations, the National Aeronautics and Space Administration (NASA) DC-8 aircraft carrying the Airborne Precipitation Radar Third Generation (APR-3) flew mostly constant altitude flights above the University of North Dakota Citation aircraft. The Citation was outfitted with instruments that measured state parameters (e.g., temperature and pressure), bulk cloud properties (e.g., total water content [TWC]), and particle size distribution (PSD). The APR-3 observations allowed for simultaneous scanning measurements of K_u - (13.4 GHz), K_a - (35.6 GHz), and W - (94.9 GHz) band reflectivity $\pm 25^\circ$ from nadir with 30-m vertical sampling. Measured reflectivity values were corrected for attenuation and adjusted for calibration using the method described in section 2.4.

2.2. Microphysics

The PSD was measured onboard the Citation using a combination of two optical array probes: the vertically oriented array of a two-dimensional stereo (2DS) probe and a vertically oriented high volume precipitation spectrometer version 3 (HVPS3). To minimize the influence of shattered artifacts in the PSDs, both the 2DS and HVPS3 had antishattering tips, and the data were processed with the University of Illinois/Oklahoma

Optical Array Probe Processing Software, using particle interarrival times to identify shattered artifacts from the 2DS data (Field et al., 2003; Jackson et al., 2014). Here the 2DS is used to determine the number distribution function, $N(D)$, for particles with D , which is defined as the diameter of the minimum enclosing circle of the projected 2D image, between 225 μm and 1 mm, while the HVPS3 is used for D between 1 mm and 3.25 cm. The lower bound for the $N(D)$ using the 2DS is chosen based on the observation of supercooled drizzle drops ($D \cong 200 \mu\text{m}$; Figure 2g), which ensures that calculations using the PSD are mostly characteristic of ice. Further, the absence of smaller particles should not have a major impact on calculated ice mass or reflectivity, which are dominated by larger particles. A 5-s moving average of the PSD is applied 2 s before and after each point when and where the Citation aircraft is regarded as coincident with a radar gate (section 2.3).

Several bulk microphysical quantities are calculated from the PSD in order to evaluate the retrieval of ρ_e and characteristic size. For this study, ρ_e is the ratio of the mass of ice to the total volume of ice (V) within some sample volume. Since there is no method of directly deriving ρ_e from two-dimensional images obtained by the 2DS and HVPS3, it is defined as

$$\rho_e = \frac{IWC}{V}, \quad (1)$$

where V is defined as the sum of the volume enclosed by an oblate spheroid with an aspect ratio, α , of 0.6 (Hogan et al., 2012) of all particles within the PSD and IWC is the ice water content from all particles within the PSD. Mathematically, V can be described as

$$V = \frac{\pi}{6} \int_{D_{\min}}^{D_{\max}} N(D) \alpha D^3 dD, \quad (2)$$

and IWC as

$$IWC = \int_{D_{\min}}^{D_{\max}} N(D) a D^b dD. \quad (3)$$

The calculation of IWC from the PSD requires a mass-dimension (m - D) relation that provides the a and b values in equation (3). To investigate the sensitivity of the computed IWC to the choice of relation, two relationships are used here and discussed in section 2.4: Brown and Francis (1995) modified by converting its original particle size definitions to D following Hogan et al. (2012) with $a = 0.0121 \text{ kg/m}^b$ and $b = 1.9$ (hereafter BF95); and Heymsfield et al. (2004) with $a = 0.0061 \text{ g/cm}^b$ and $b = 2.05$ (hereafter HY04).

The characteristic size chosen for this study is the median mass dimension (D_{mm}), which is defined as the dimension where 50% of the accumulated IWC is less than D_{mm} and 50% greater than D_{mm} . The in situ derived D_{mm} will be used to evaluate the relationship between D_{mm} and DFR suggested by Kneifel et al. (2015) and shown in section 3.2.

2.3. Colocating Radar and In Situ Observations

Fifteen flight legs with temperatures lower than -0.5°C within stratiform clouds were sampled representing 2.2 hr of cloud observations when the APR-3 aboard the DC-8 sampled the same region as the Citation. In situ observations were assumed to be characteristic of the entire matched radar volume despite the differences in sample volume between the radar and the in situ probes. Here radar volumes collected within 10 min temporally and 1 km spatially of the Citation are regarded as collocated. Furthermore, analysis is restricted to periods when the total number concentration (N_t) was greater than 10^3 m^{-3} to ensure that the Citation was within cloud.

To find the instances of collocation, the k -dimensional tree searching algorithm from the open-source SciPy software package (Oliphant, 2007, leafsize = 16) was used to obtain the closest 30 radar gates within 1 km of the Citation location. Any radar gate contaminated by the radar signature of the Citation or any other outlier (e.g., spurious measurement) was removed using the following statistical definition of an outlier:

$$\text{Outlier} > \text{Median} + 1.5 \times \text{Interquartile range} \quad (4)$$

$$\text{Outlier} < \text{Median} - 1.5 \times \text{Interquartile range} \quad (5)$$

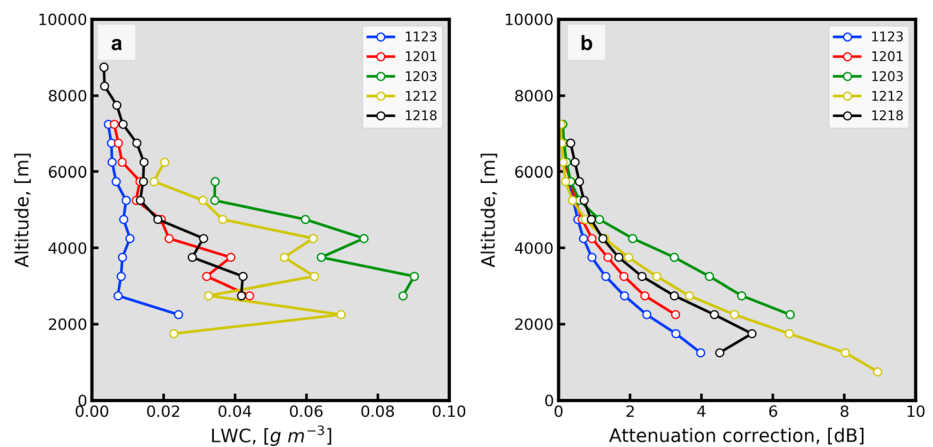


Figure 1. Attenuation correction method. (a) Observed supercool liquid water (LWC) measured by King hot wire probe as a function of altitude. Each line represents the median LWC for 500-m bins with temperatures less than -5°C . The colors correspond to the dates indicated in the legend. (b) The cumulative median applied correction for W -band reflectivity as a function of altitude on each flight day.

The Barnes (1964) interpolation technique with a weighting factor of $\kappa = 1,000\ \text{m}^2$ (Trapp & Doswell, 2000) was then applied to provide a characteristic radar measurement. If the standard deviation of the 30 gates was greater than 3 dBZ, the cloud element was regarded as heterogeneous, and the point was not used in the analysis of section 3. For additional quality control, the bright band, rain echoes, radar artifacts, and the surface return were identified and removed from the radar data before matching. To test the sensitivity to the number of gates used in the average, the difference between using the closest gate and 30 gates was calculated and was on average less than 0.1 dBZ (see Figure S1).

2.4. Calibration and Attenuation Correction

Calibration of the measured reflectivity at the three frequencies is required before analysis of DFR can be conducted. In theory, the same reflectivity should be measured for all three frequencies for small ice particles near cloud top where attenuation is low and particles scatter in the Rayleigh regime. Data between 10 and 15 dBZ near echo top were used to compare the K_u band to the K_a band, and data between -10 and 0 dBZ were used to compare K_a to W band. Additionally, clear air observations of the ocean surface backscatter cross section (Tanelli et al., 2006) are used to assess the K_u -band absolute calibration. The relative uncertainty in calibration is estimated to be 0.5 to 1 dB for K_u - K_a and K_a - W , respectively.

To compare the observed multifrequency radar observations with in situ data on the DFR plane against scattering models, a correction for two-way attenuation at the W band caused by supercool liquid water (LWC), atmospheric constituents (e.g., O_2), and ice scattering must be performed. Corrections based on path-integrated attenuation are not possible for the flight legs examined because some flights were over complex terrain (where the surface reference technique to estimate path-integrated attenuation is not sufficiently reliable). Thus, to correct for the absorption due to LWC, in situ measurements of LWC observed by the King probe for each flight are used to create a median profile of LWC (Figure 1a), which is then used to calculate the specific attenuation using the coefficients from Meneghini and Kozu (1990). It is noted that the King probe could overestimate LWC because of its interaction with ice (e.g., Cober et al., 2001) and underestimate LWC in the presence of drizzle drops (e.g., Schwarzenboeck et al., 2009; Strapp et al., 2003). No correction is applied to the LWC due to these uncertainties. Path-integrated attenuation due to LWC is estimated to be on the order of 1–1.5 dB. To correct for absorption from atmospheric water vapor and diatomic oxygen, the coefficients from the 2013 manual by the Radiocommunication Sector of International Telecommunication Union and radiosonde data from Quillayute Airport, near the coast of Washington State, closest in time to the beginning of each flight leg, are used. The correction magnitude for gaseous absorption above the melting level is estimated to be on the order of 1 dB. Correction for extinction from ice scattering at W band (negligible at the other frequencies) is performed using Kulie et al. (2014) relating extinction and K_u -band reflectivity factor. The correction from ice extinction makes up the remaining total attenuation correction shown in Figure 1b.

Median path-integrated attenuation correction at W band is estimated to be on the order of 3.5–9 dB. Attenuation correction at the other wavelengths (K_u and K_a bands) is only preformed for the atmospheric gases and is on the order of 0.1 and 0.5 dB for K_u and K_a bands, respectively.

2.5. Matched Particle Size Distribution Representativeness

In order to assess how well the matched PSD and the subsequent calculations of D_{mm} and ρ_e represent particles within the radar gates, the K_u -band reflectivity is forward modeled from the observed PSD using the Rayleigh-Gans spheroidal approximation (Hogan et al., 2012) and the m - D relations noted in section 2.2. The K_u band is chosen because it experiences the least amount of attenuation and non-Rayleigh scattering effects. Calculated reflectivity using BF95 has a persistent underestimation when compared to the coincident K_u band radar reflectivity with a mean difference of -7.1 dB and a correlation coefficient of 0.71. The same comparison using the m - D from HY04 provides an improved match with a mean difference of $+1.4$ dB and a correlation coefficient of 0.72 (see Figure S2). Given the low overall bias found, the HY04 relation is used henceforth to calculate the D_{mm} and ρ_e . Although ground-based observations have shown that the m - D can change quickly in time (von Lerber et al., 2017), the HY04 relation provides limited bias in forward modeled reflectivities supporting the use of a single m - D .

3. Results and Discussion

3.1. Case Study: 3 December 2015

On 3 December 2015, stratiform prefrontal precipitation over the Olympic Mountains produced 24-hr rain totals greater than 200 mm on the southern slopes and around 70 mm in the western valleys. Airborne radar observations (Figures 2a–2c) show a bright band at around 2.5 km above mean sea level (ASL) and echo tops near 8 km ASL. The Citation sampled a region around 4 km ASL and at -12.5 °C just over the high terrain of the Olympic Mountains. The flight started over the southeast portion of the Olympic Mountains where the low-level flow was quasi-orthogonal to the mountain slopes, producing the strongest orographic forcing. This is hypothesized to explain why supercooled drizzle drops were found here (Figure 2g). Most collocated triple-frequency radar observations for this case were on the portion of the DFR plane where scattering models of spherical particles and rimed aggregates coexist. Thus, separation of aggregates from spheroidal particles cannot be unambiguously determined from the DFR plane (Figure 2d; polygon with black shading). At 15:19:44 UTC, matched radar gates at the Citation show DFR_{Ka-W} of 10.9 dB and DFR_{Ku-Ka} of 3.1 dB (Figure 2d, blue). Example coincident images from the HVPS3, chosen using a random number generator, resemble quasi-spherical particles (Figure 2e, blue). The D_{mm} is 1.36 mm and ρ_e is 0.1 g/cm³ at this time. Over the next 5 min as the Citation flew NW, the DFR_{Ka-W} decreased to 5.9 dB while the DFR_{Ku-Ka} remained at similar values (3.2 dB; yellow Figure 2d). Particle images over this 5-min period became less spherical and larger, with D_{mm} rising to 2.6 mm and ρ_e decreasing to 0.05 g/cm³.

Modeling results from Leinonen and Szyrmer (2015) suggest that as the degree of riming of aggregates increases, increasing ρ_e , the DFR_{Ka-W} should increase due to more non-Rayleigh scattering effects at W band. The case presented here is consistent with this trend, showing that as the observed DFR_{Ka-W} decreases and the DFR_{Ku-Ka} remains the same, ρ_e decreases. Furthermore, both the HVPS3 particle images and measured liquid water content support the notion of increased riming, showing more compact particles (Figure 2e) and increased liquid water content (0.1 to 0.2 g/m³, respectively) at 15:19:44 UTC compared to 15:24:14 UTC.

3.2. DFR Plane and Bulk Statistics

To evaluate ρ_e and D_{mm} in the DFR plane, all coincident DFR microphysical in situ observations from OLYMPEx are shown in Figure 3. Coincident observations throughout the atmospheric column correspond to temperatures from -30 to -0.5 °C (Figure 3a). The most frequent DFR bin, using 1-dB bins, of all 7,948 observations is found inside the spheroidal-behavior region characterized by DFR_{Ku-Ka} of 0 dB and DFR_{Ka-W} of 2 dB (Figure 3b, black outlined bin). Furthermore, 31% of the OLYMPEx DFR data within stratiform clouds are found on the DFR plane where only unrimed aggregate and large rimed aggregates scattering models exist. Coincident ρ_e and D_{mm} calculated from the PSD (Figures 3c and 3d) present the average bulk properties for the same 1-dB frequency histogram bins as in Figure 3b. The most frequent bin (outlined in black) is characterized by a mean ρ_e of 0.12 g/cm³ and a mean D_{mm} of 0.85 mm. The most frequent

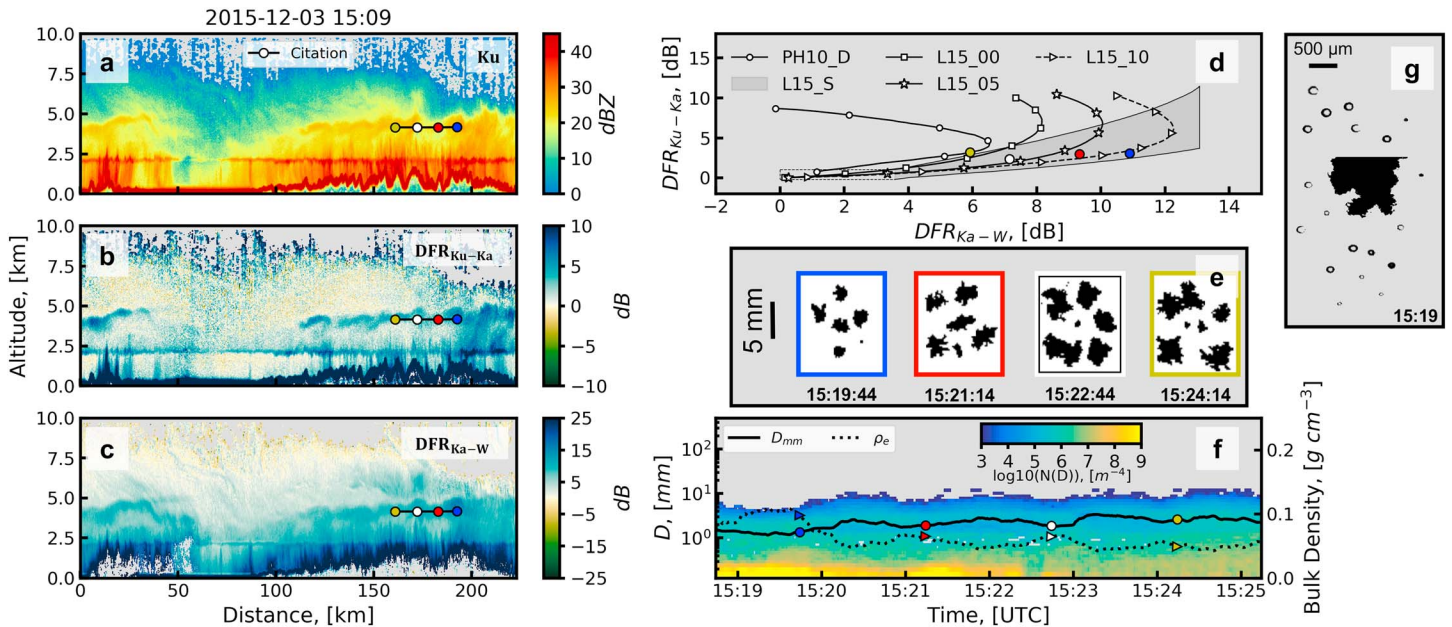


Figure 2. Vertical cross section of (a) K_u -band reflectivity, (b) DFR_{Ku-Ka} , (c) DFR_{Ka-W} measured by the Airborne Precipitation Radar Third Generation (corrected following section 2.4), with University of North Dakota Citation track overlaid with a colored marker every 90 s corresponding to colors in other subplots. Colors in order of time are blue, red, white, and yellow. (d) DFR plane containing scattering model curves of a dendrite aggregate (PH10_D) adapted from Petty and Huang (2010), dendrite aggregates with 0, 0.5, and 1 kg/m^2 of rime ice (L15_00, L15_05, and L15_10, respectively) adapted from Leinonen and Szyrmer (2015), and 90% of spheroid approximation for aggregates (L15_S, black shaded) adapted from Leinonen and Szyrmer (2015). The polygon is the inferred region where both complex and simple scattering models exist. Colored points are 10-s means of matched DFR values at markers in Figures 2a–2c. (e) Randomly selected HVPS3 particle images corresponding to the colors/times from Figure 2d. (f) $N(D)$ (shading), D_{mm} (solid circles), and ρ_e (dotted triangles) along the flight track of the Citation in Figures 2a–2c. (g) Sample 2DS images from 15:19, showing numerous out of focus spherical particles, inferred to be supercooled drizzle drops.

occurrence supports a conclusion of frequent smaller and higher ρ_e particles, potentially pristine/nonaggregated particles or small rimed aggregates within the OLYMPLEX stratiform clouds. Furthermore, observations well outside the spheroidal-behavior region (polygon), with $DFR_{Ku-Ka} \geq 5$ dB and $DFR_{Ka-W} \leq 5$, (Figure 3c) show larger D_{mm} , lower ρ_e particles observed at higher temperatures ($T \cong -0.5$ °C), which provide evidence of aggregate-like particles. For example, a particle image from the HVPS3 is included on Figure 3c, showing a large ($D \cong 20$ mm) aggregate-like particle representative of a $DFR_{Ku-Ka} \geq 10$ dB and a DFR_{Ka-W} of ~ 4 dB. To contrast this image, additional example particle images from the HVPS3 (Figure 3d) at a similar DFR_{Ka-W} but $DFR_{Ku-Ka} \leq -1$ dB indicates smaller ($D \cong 2$ mm), more spherical particles. While a negative DFR_{Ku-Ka} is not predicted by theoretical models, this is most likely a result of the calibration of the radars, radar measurement precision (which by itself accounts for a measurement uncertainty of about 0.7 dB rms in the case of APR-3), the attenuation correction, or the colocation technique.

Comparing the results from Figure 3 to past studies, the majority (63%) of OLYMPLEX observations being found within the spheroidal-behavior region of the DFR plane (Figures 3a and 3b) is consistent with prior airborne radar observations (Kulie et al., 2014) and spaceborne radar observations (Yin et al., 2017). This is expected when the particles in the PSD are scattering in the Rayleigh regime at all three frequencies ($DFR_{Ku-Ka} \cong DFR_{Ka-W}$). However, 54% of OLYMPLEX PSDs with larger particles ($D_{mm} \geq 2$ mm) are also found in the spheroidal-behavior region. Moreover, Figures 3c and 3d provide additional support for the results from Kneifel et al. (2015), showing that (1) ρ_e increases as DFR_{Ku-Ka} decreases and DFR_{Ka-W} increases and (2) D_{mm} increases further from the origin of the DFR plane. The ability to retrieve ρ_e from the DFR plane is demonstrated in Figure 3c, but these observational results do indicate some inconsistency from regions on the DFR plane in the literature (e.g., Kneifel et al., 2015; Leinonen & Moisseev, 2015). Figure 3c supports the results from the observational study of Kneifel et al. (2015), resembling the rotation of their DFR scattering curves, but does not show the expected covariation of ρ_e with DFR_{Ka-W} that is shown in the modeling

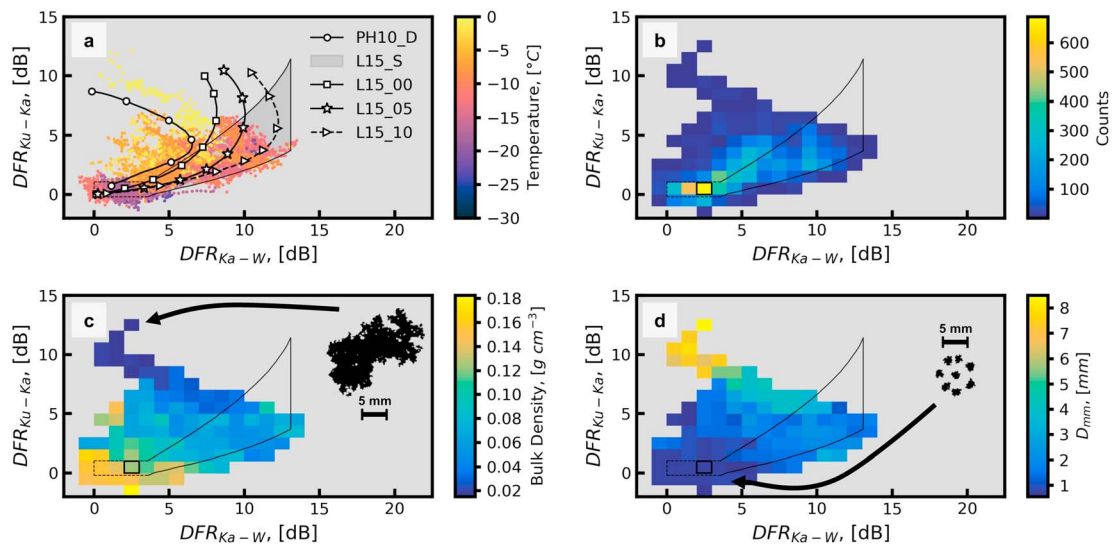


Figure 3. DFR plane using all 15 matched flight legs. (a) Scatterplot of all matched instances between the Airborne Precipitation Radar Third Generation and the Citation colored by observed temperature. Curves and polygon are the same as in Figure 2d. (b) Joint frequency of occurrence of DFR_{Ku-Ka} versus DFR_{Ka-W} , most frequent bin outlined in black. The polygon outlines the region where particle shape is ambiguous. (c) Using the identical two-dimensional histogram in Figure 3b, but bins are colored by the mean ρ_e within the bin. Black silhouette is an example particle image from the HVPS3 at the indicated region on the DFR plane. (d) Idem Figure 3c but colored by mean D_{mmm} in each bin. Black silhouettes are particle images from the HVPS3 at the indicated region on the DFR plane.

results from Leinonen and Szyrmer (2015). This could be a result of the constant m - D assumption since modeling studies assume the m - D relation changes with the degree of riming and, consequently, so does ρ_e . However, the accretion of rime ice and its effect on the m - D and scattering properties are difficult to observe. In order to incorporate a variant m - D relation, improved measurements of ice particle mass are required, especially when the PSD contains large ($D > 4$ mm) particles (Korolev et al., 2013).

4. Conclusions

Data collected in late 2015 during OLYMPEx (Houze et al., 2017) represent a first-of-its-kind data set of airborne triple-frequency radar measurements coincident with airborne microphysical observations. A first-order liquid, gas, and ice attenuation correction of the W -band reflectivity using in situ observations (section 2.4) allows for the direct evaluation of past work on triple-frequency radar snow/ice property retrievals (e.g., Kneifel et al., 2011, 2015; Leinonen & Szyrmer, 2015).

In situ particle images obtained on 3 December 2015 coincident with triple-frequency radar observations show that distinction among particle types cannot be unambiguously retrieved since radar observations were found within a region outlined by scattering models of both rimed aggregates and spheroids (polygon, Figure 2d). However, the bulk statistics of 15 flight legs reveal that 31% of the collected OLYMPEx in-cloud observations are found on the DFR_{Ku-Ka} - W plane where only unrimed aggregate or large rimed aggregate scattering models exist.

Previous modeling studies show that aggregates scatter differently than spheroidal particles but require unrimed aggregates (e.g., Kneifel et al., 2011; Leinonen & Moisseev, 2015) or large rimed aggregates (e.g., Leinonen & Szyrmer, 2015) to be present. If unrimed aggregates or large rimed aggregates are infrequent (occur 31% of the time) throughout the atmospheric column, then the benefits of using the DFR plane to retrieve information to constrain a priori assumptions in the precipitation rate of ice (R) and the ice water content (IWC) retrievals might be limited. Triple-frequency observations from other studies (Kulie et al., 2014; Yin et al., 2017) also show that observations are more frequently found in the spheroidal-behavior region. Furthermore, the uncertainty in correcting for ice and liquid water extinction without coincident in situ measurements, the latter of which may be highly variable and not correlated with radar reflectivity in the column, may hamper the ability of retrievals using W band to differentiate particle habit. However, other

meteorological regimes (e.g., less supercooled liquid water) may yield a more comprehensive evaluation of the potential of triple-frequency retrievals.

In terms of evaluating the ability of DFR retrievals of bulk particle properties, it is found that

1. The case study on 3 December 2015 shows in situ bulk effective density (ρ_e) increases with increasing coincident measurements of $DFR_{Ka} - W$ (Figure 2d).
2. Bulk effective density from all coincident points generally increases with decreasing $DFR_{Ku} - Ka$ (Figure 3c).
3. Median mass dimension (D_{mm}) increases away from the origin of the DFR plane, with increasing $DFR_{Ku} - Ka$ and $DFR_{Ka} - W$ (Figure 3d).

These results support the retrieval of D_{mm} and ρ_e using triple-frequency radar observations with the acknowledgment that a single m - D relation was used to approximate particle mass. Additional independent observations of single particle masses are needed to reduce uncertainty in deriving a time-dependent variant m - D relation, especially when large (particle diameter > 4 mm) particles are present in the PSD. Despite the uncertainties, information on these key bulk microphysical parameters are included in the $DFR_{Ku} - Ka$ and $DFR_{Ka} - W$, with more information regarding D_{mm} and ρ_e suggested in $DFR_{Ku} - Ka$. Since the Global Precipitation Measurement (GPM, Hou et al., 2014) mission collects $DFR_{Ku} - Ka$, there is potential for developing improved ice cloud property retrievals for the GPM mission as well as for future multifrequency ground- and satellite-based radar measurements since currently in the GPM's algorithms ρ_e is assumed to be quasi-constant with a value of 0.1 g/cm^3 (Seto et al., 2013).

Acknowledgments

Funding for this research was provided by NASA Precipitation Measurement Missions grant NNX16AD80G under Ramesh Kakar. A portion of the research described in this paper was carried out at the Jet Propulsion Laboratory, California Institute of Technology, under contract with the National Aeronautics and Space Administration. We thank all the participants of OLYMPEx for collecting the data used in this study. All data used in this investigation are found on the NASA GHRC OLYMPEx data archive <https://doi.org/10.5067/GPMGV/OLYMPEx/DATA101>. The matching software to match the Citation and the radar gates can be found here <https://zenodo.org/badge/latestdoi/113089990>.

References

- Austin, R. T., Heymsfield, A. J., & Stephens, G. L. (2009). Retrieval of ice cloud microphysical parameters using the CloudSat millimeter-wave radar and temperature. *Journal of Geophysical Research*, 114, D00A23. <https://doi.org/10.1029/2008JD010049>
- Barnes, S. L. (1964). A technique for maximizing details in numerical weather map analysis. *Journal of Applied Meteorology*, 3(4), 396–409. [https://doi.org/10.1175/1520-0450\(1964\)003%3C0396:ATFMDI%3E2.0.CO;2](https://doi.org/10.1175/1520-0450(1964)003%3C0396:ATFMDI%3E2.0.CO;2)
- Brown, P. R. A., & Francis, P. N. (1995). Improved measurements of the ice water content in cirrus using a total-water probe. *Journal of Atmospheric and Oceanic Technology*, 12(2), 410–414. [https://doi.org/10.1175/1520-0426\(1995\)012%3C0410:IMOTIW%3E2.0.CO;2](https://doi.org/10.1175/1520-0426(1995)012%3C0410:IMOTIW%3E2.0.CO;2)
- Cober, S. G., Isaac, G. A., Korolev, A. V., & Strapp, J. W. (2001). Assessing cloud-phase conditions. *Journal of Applied Meteorology*, 40(11), 1967–1983. [https://doi.org/10.1175/1520-0450\(2001\)040%3C1967:ACPC%3E2.0.CO;2](https://doi.org/10.1175/1520-0450(2001)040%3C1967:ACPC%3E2.0.CO;2)
- Delanoë, J., Hogan, R. J., Forbes, R. M., Bodas-Salcedo, A., & Stein, T. H. M. (2011). Evaluation of ice cloud representation in ECMWF and UK Met Office models using CloudSat and CALIPSO data. *Quarterly Journal of the Royal Meteorological Society*, 137(661), 2064–2078. <https://doi.org/10.1002/qj.882>
- Field, P. R., Wood, R., Brown, P. R. A., Kaye, P. H., Hirst, E., Greenaway, R., & Smith, J. A. (2003). Ice particle interarrival times measured with a fast FSP. *Journal of Atmospheric and Oceanic Technology*, 20(2), 249–261. [https://doi.org/10.1175/1520-0426\(2003\)020%3C0249:IPITMW%3E2.0.CO;2](https://doi.org/10.1175/1520-0426(2003)020%3C0249:IPITMW%3E2.0.CO;2)
- Heymsfield, A. J., Bansemmer, A., Schmitt, C., Twohy, C., & Poellot, M. R. (2004). Effective ice particle densities derived from aircraft data. *Journal of the Atmospheric Sciences*, 61(9), 982–1003. [https://doi.org/10.1175/1520-0469\(2004\)061%3C0982:EIPDDF%3E2.0.CO;2](https://doi.org/10.1175/1520-0469(2004)061%3C0982:EIPDDF%3E2.0.CO;2)
- Hogan, R. J., Tian, L., Brown, P. R. A., Westbrook, C. D., Heymsfield, A. J., & Eastment, J. D. (2012). Radar scattering from ice aggregates using the horizontally aligned oblate spheroid approximation. *Journal of Applied Meteorology and Climatology*, 51(3), 655–671. <https://doi.org/10.1175/JAMC-D-11-074.1>
- Hou, A. Y., Kakar, R. K., Neeck, S., Azarbarzin, A. A., Kummerow, C. D., Kojima, M., et al. (2014). The global precipitation measurement mission. *Bulletin of the American Meteorological Society*, 95(5), 701–722. <https://doi.org/10.1175/BAMS-D-13-00164.1>
- Houze, R. A. Jr., McMurdie, L. A., Petersen, W. A., Schwaller, M. R., Baccus, W., Lundquist, J. D., et al. (2017). The Olympic Mountains Experiment (OLYMPEx). *Bulletin of the American Meteorological Society*, 98(10), 2167–2188. <https://doi.org/10.1175/BAMS-D-16-0182.1>
- Jackson, R. C., McFarquhar, G. M., Stith, J., Beals, M., Shaw, R. A., Jensen, J., et al. (2014). An assessment of the impact of antishattering tips and artifact removal techniques on cloud ice size distributions measured by the 2D cloud probe. *Journal of Atmospheric and Oceanic Technology*, 31(12), 2567–2590. <https://doi.org/10.1175/JTECH-D-13-00239.1>
- Kneifel, S., Kulie, M. S., & Bennartz, R. (2011). A triple-frequency approach to retrieve microphysical snowfall parameters. *Journal of Geophysical Research*, 116, D11203. <https://doi.org/10.1029/2010JD015430>
- Kneifel, S., von Lerber, A., Tiira, J., Moiseev, D., Kollias, P., & Leinonen, J. (2015). Observed relations between snowfall microphysics and triple-frequency radar measurements. *Journal of Geophysical Research: Atmospheres*, 120, 6034–6055. <https://doi.org/10.1002/2015JD023156>
- Korolev, A., Strapp, J. W., Isaac, G. A., & Emery, E. (2013). Improved airborne hot-wire measurements of ice water content in clouds. *Journal of Atmospheric and Oceanic Technology*, 30(9), 2121–2131. <https://doi.org/10.1175/JTECH-D-13-00007.1>
- Kulie, M. S., Hiley, M. J., Bennartz, R., Kneifel, S., & Tanelli, S. (2014). Triple-frequency radar reflectivity signatures of snow: Observations and comparisons with theoretical ice particle scattering models. *Journal of Applied Meteorology and Climatology*, 53(4), 1080–1098. <https://doi.org/10.1175/JAMC-D-13-066.1>
- Leinonen, J., Kneifel, S., Moiseev, D., Tyynelä, J., Tanelli, S., & Nousiainen, T. (2012). Evidence of non-spheroidal behavior in millimeter-wavelength radar observations of snowfall. *Journal of Geophysical Research*, 117, D18205. <https://doi.org/10.1029/2012JD017680>
- Leinonen, J., & Moiseev, D. (2015). What do triple-frequency signatures reveal about aggregate snowflakes? *Journal of Geophysical Research: Atmospheres*, 120, 229–239. <https://doi.org/10.1002/2014JD022072>
- Leinonen, J., & Szyrmer, W. (2015). Radar signatures of snowflake riming: A modeling study. *Earth and Space Science*, 2, 346–358. <https://doi.org/10.1002/2015EA000102>
- Matrosov, S. Y. (2007). Modeling backscatter properties of snowfall at millimeter wavelengths. *Journal of the Atmospheric Sciences*, 64(5), 1727–1736. <https://doi.org/10.1175/JAS3904.1>

- Meneghini, R., & Kozu, T. (1990). *Spaceborne weather radar*. Boston: Artech House.
- Oliphant, T. E. (2007). Python for scientific computing. *Computing in Science & Engineering*, 9(3), 10–20. <https://doi.org/10.1109/MCSE.2007.58>
- Petty, G. W., & Huang, W. (2010). Microwave backscatter and extinction of soft ice spheres and complex snow aggregates. *Journal of the Atmospheric Sciences*, 67(3), 769–787. <https://doi.org/10.1175/2009JAS3146.1>
- Schwarzenboeck, A., Mioche, G., Armetta, A., Herber, A., & Gayet, J.-F. (2009). Response of the Nevzorov hot wire probe in clouds dominated by droplet conditions in the drizzle size range. *Atmospheric Measurement Techniques*, 2(2), 779–788. <https://doi.org/10.5194/amt-2-779-2009>
- Seto, S., Iguchi, T., & Oki, T. (2013). The basic performance of a precipitation retrieval algorithm for the Global Precipitation Measurement mission's single/dual-frequency radar measurements. *IEEE Transactions on Geoscience and Remote Sensing*, 51(12), 5239–5251. <https://doi.org/10.1109/TGRS.2012.2231686>
- Stein, T. H. M., Parker, D. J., Hogan, R. J., Birch, C. E., Holloway, C. E., Lister, G. M. S., et al. (2015). The representation of the West African monsoon vertical structure in the Met Office Unified Model: An evaluation with CloudSat. *Quarterly Journal of the Royal Meteorological Society*, 141(693), 3312–3324. <https://doi.org/10.1002/qj.2614>
- Strapp, J. W., Oldenburg, J., Ide, R., Lilie, L., Bacic, S., Vukovic, Z., et al. (2003). Wind tunnel measurements of the response of hot-wire liquid water content instruments to large droplets. *Journal of Atmospheric and Oceanic Technology*, 20(6), 791–806. [https://doi.org/10.1175/1520-0426\(2003\)020%3C0791:WTMOTR%3E2.0.CO;2](https://doi.org/10.1175/1520-0426(2003)020%3C0791:WTMOTR%3E2.0.CO;2)
- Tanelli, S., Durden, S. L., & Im, E. (2006). Simultaneous measurements of K_u - and K_a -band sea surface cross-sections by an airborne radar. *IEEE Geoscience and Remote Sensing Letters*, 3(3), 359–363. <https://doi.org/10.1109/LGRS.2006.872929>
- Trapp, R. J., & Doswell, C. A. (2000). Radar data objective analysis. *Journal of Atmospheric and Oceanic Technology*, 17(2), 105–120. [https://doi.org/10.1175/1520-0426\(2000\)017%3C0105:RDOA%3E2.0.CO;2](https://doi.org/10.1175/1520-0426(2000)017%3C0105:RDOA%3E2.0.CO;2)
- von Lerber, A., Moiseev, D., Bliven, L. F., Petersen, W., Harri, A., & Chandrasekar, V. (2017). Microphysical properties of snow and their link to $Z_e - S$ relations during BAECC 2014. *Journal of Applied Meteorology and Climatology*, 56, 1561–1582. <https://doi.org/10.1175/JAMC-D-16-0779.1>
- Yin, M., Liu, G., Honeyager, R., & Turk, F. J. (2017). Observed differences of triple-frequency radar signatures between snowflakes in stratiform and convective clouds. *Journal of Quantitative Spectroscopy & Radiative Transfer*, 193, 13–20. <https://doi.org/10.1016/j.jqsrt.2017.02.017>